

Influence of alkali and alkaline earth metal ion doping on the optical and thermal properties of Yb^{3+}/Ho^{3+} co-doped $NaBi(MoO_4)_2$ single crystals

Wenzhi Su(宿文志), Kaiming Kan(阚恺铭), Chuancheng Zhang(张传成), Yong Zou(邹勇), Shoujun Ding(丁守军), Qingli Zhang(张庆礼)

Citation: Chin. Phys. B, 2026, 35 (**8**): 088102. DOI: 10.1088/1674-1056/ae12dc
http://cpb.iphy.ac.cn; http://iopscience.iop.org/cpb

What follows is a list of articles you may be interested in

Understanding the synergistic effect of mixed solvent annealing on perovskite film formation

Kun Qian(钱昆), Yu Li(李渝), Jingnan Song(宋静楠), Jazib Ali, Ming Zhang(张明), Lei Zhu(朱磊), Hong Ding(丁虹), Junzhe Zhan(詹俊哲), and Wei Feng(冯威)

Chin. Phys. B, 2021, 30 (**6**): 068103. DOI: 10.1088/1674-1056/abdb1f

Vertical GaN Shottky barrier diode with thermally stable TiN anode

Da-Ping Liu(刘大平), Xiao-Bo Li(李小波), Tao-Fei Pu(蒲涛飞), Liu-An Li(李柳暗), Shao-Heng Cheng(成绍恒), and Qi-Liang Wang(王启亮)

Chin. Phys. B, 2021, 30 (**3**): 038101. DOI: 10.1088/1674-1056/abc547

Characteristics of urea under high pressure and high temperature

Shuai Fang(房帅), Hong-An Ma(马红安), Long-Suo Guo(郭龙锁), Liang-Chao Chen(陈良超), Yao Wang(王遥), Lu-Yao Ding(丁路遥), Zheng-Hao Cai(蔡正浩), Jian Wang(王健), Xiao-Peng Jia(贾晓鹏)

Chin. Phys. B, 2019, 28 (**9**): 098101. DOI: 10.1088/1674-1056/ab3445

Effect of sintering temperature on luminescence properties of borosilicate matrix blue-green emitting color conversion glass ceramics

Qiao-Yu Zheng(郑巧瑜), Yang Li(李杨), Wen-Juan Wu(吴文娟), Ming-Ming Shi(石明明), Bo-Bo Yang(杨波波), Jun Zou(邹军)

Chin. Phys. B, 2019, 28 (**10**): 108102. DOI: 10.1088/1674-1056/ab3f97

Excellent thermal stability and thermoelectric properties of *Pnma*-phase SnSe in middle temperature aerobic environment

Yu Tang(唐语), Decong Li(李德聪), Zhong Chen(陈钟), Shuping Deng(邓书平), Luqi Sun(孙璐琪), Wenting Liu(刘文婷), Lanxian Shen(申兰先), Shukang Deng(邓书康)

Chin. Phys. B, 2018, 27 (**11**): 118105. DOI: 10.1088/1674-1056/27/11/118105

Influence of alkali and alkaline earth metal ion doping on the optical and thermal properties of Yb^{3+}/Ho^{3+} co-doped $NaBi(MoO_4)_2$ single crystals

Wenzhi Su(宿文志)[1,2,†], Kaiming Kan(阚恺铭)[1,2,†], Chuancheng Zhang(张传成)[1,2,3], Yong Zou(邹勇)[1,2], Shoujun Ding(丁守军)[1,2,‡], and Qingli Zhang(张庆礼)[4]

[1] *School of Microelectronics and Data Science, Anhui University of Technology, Maanshan* 243002, *China*
[2] *Anhui Provincial Joint Key Laboratory of Disciplines for Industrial Big Data Analysis and Intelligent Decision, Maanshan* 243002, *China*
[3] *University of Science and Technology of China, Hefei* 230026, *China*
[4] *Anhui Institute of Optics and Fine Mechanics, Chinese Academy of Sciences, Hefei* 230031, *China*

(Received 28 August 2025; revised manuscript received 10 October 2025; accepted manuscript online 14 October 2025)

The influence of alkali and alkaline earth metal ion doping on the upconversion (UC) luminescence properties of Yb^{3+}, Ho^{3+} co-doped $NaBi(MoO_4)_2$ (NBM) single crystals was systematically investigated. A series of Yb^{3+}, Ho^{3+}:NBM single crystals doped with Li^+, K^+, and Ca^{2+} ions were successfully grown using the Czochralski method. Their structural characteristics were analyzed through x-ray diffraction (XRD), transmission spectroscopy, and scanning electron microscopy (SEM), confirming a tetragonal crystal structure with space group $I4_1/a$. Under 980 nm and 450 nm laser excitation, the crystals exhibited distinct UC emission profiles, with dominant red and green emissions, respectively. Tauc plot analysis indicated that Ca^{2+} doping introduced donor levels within the crystal lattice, effectively narrowing the optical bandgap. Power-dependent luminescence studies revealed that both red and green UC emissions originated from two-photon excitation processes. Temperature-dependent photoluminescence measurements under both excitation wavelengths demonstrated that co-doping with Li^+, K^+, and Ca^{2+} significantly enhanced the thermal stability of the luminescent properties. Furthermore, variable-temperature fluorescence lifetime analyses showed that alkali and alkaline earth metal ion doping effectively mitigated the luminescence lifetimes. Overall, the incorporation of Li^+, K^+, and Ca^{2+} ions was found to markedly improve both the UC luminescence intensity and thermal robustness of Yb^{3+}, Ho^{3+}:NBM single crystals, offering promising prospects for high-performance luminescent materials.

Keywords: $NaBi(MoO_4)_2$ crystal, upconversion luminescence, thermal stability, alkali ion co-doping, alkaline earth metal ion co-doping

PACS: 81.10.Fq, 78.55.–m, 87.15.mq, 61.43.–j

DOI: 10.1088/1674-1056/ae12dc **CSTR:** 32038.14.CPB.ae12dc

1. Introduction

Upconversion (UC) luminescence refers to a nonlinear optical phenomenon operating on the anti-Stokes principle. In this process, a luminescent center takes in two or more low-energy photons, one after another, and then emits a single high-energy photon that has a shorter wavelength compared to the excitation source.[1–6] Over the past few decades, considerable progress has been made in the synthesis and development of UC materials, particularly those doped with rare-earth (RE) ions. These materials exhibit a range of exceptional optical properties, including long fluorescence lifetimes, low autofluorescence, low toxicity, and sharp emission bands, making them ideal candidates for numerous applications. Trivalent RE ions such as Yb^{3+}, Tm^{3+}, Er^{3+}, Ho^{3+}, Pr^{3+}, and Tb^{3+} have demonstrated the ability to convert near-infrared (NIR) radiation into visible light through efficient multiphoton processes. This property has positioned RE-doped UC materials as promising platforms for applications in bioimaging, photovoltaics, optical sensors, and solid-state lasers.[7–10]

Among various host materials, molybdates have gained attention due to their favorable optical properties and potential for use in laser and phosphor technologies. In particular, double molybdate compounds with scheelite-type tetragonal symmetry have proven to be excellent hosts for luminescent ions.[11,12] Within this category, $NaBi(MoO_4)_2$ (NBM) has emerged as an especially suitable host matrix. Benefiting from the electronic characteristics of Bi^{3+}, NBM exhibits high luminescence efficiency. Moreover, its high density, rapid response time, and strong radiation resistance further enhance its suitability for advanced optical applications.[13] Previous studies have shown that NBM single crystals doped with Pr^{3+}, Nd^{3+}, Ho^{3+}, and Er^{3+} can be successfully grown using the Czochralski method, yielding excellent photoluminescent performance.[14–17]

To enhance the UC luminescence intensity of RE-doped materials, researchers have explored both external and internal

[†]These authors contributed equally to this work.
[‡]Corresponding author. E-mail: sjding@ahut.edu.cn
© 2026 Chinese Physical Society and IOP Publishing Ltd. All rights, including for text and data mining, AI training, and similar technologies, are reserved.

structural modification strategies. External approaches include core–shell engineering and metal-enhanced fluorescence via surface plasmon resonance.[18] Among these, ion doping has emerged as a straightforward and effective method for optimizing luminescent properties. In particular, alkali metal ions such as Li^+, Na^+, and K^+, as well as alkaline earth metals like Ca^{2+} and Mg^{2+}, have shown great potential for enhancing UC efficiency. Their relatively small ionic radii allow them to occupy interstitial or substitutional lattice sites, effectively altering local crystal field symmetry and promoting radiative transitions.[19] Numerous studies have confirmed the positive effects of alkali and alkaline earth metal doping on luminescence enhancement.[20–23] For example, Maurya *et al.* demonstrated that alkali ions such as Li^+, Na^+, and K^+ improve emission intensity by increasing crystal quality and reducing defects.[24] Similarly, Mg^{2+} doping in Ho^{3+}, Yb^{3+} co-doped $CaZrO_3$ significantly enhanced green light emission.[25] Luitei *et al.* reported that co-doping $CaMoO_4$:Tm^{3+}, Yb^{3+} phosphors with K^+ ions resulted in the highest UC intensity due to increased crystal field asymmetry.[26] These findings reinforce the notion that tailored doping with specific ions can effectively modulate the optical performance of UC materials.

In this work, a series of Yb^{3+}, Ho^{3+} co-doped NBM single crystals co-doped with Li^+, K^+, and Ca^{2+} ions were successfully grown using the Czochralski method. The phase structure, optical properties, and UC emission behaviors of the resulting crystals were systematically investigated under varying excitation power densities and temperature conditions. Special attention was given to the role of alkali and alkaline earth metal ions in enhancing thermal stability and UC luminescence intensity. The results demonstrate that the incorporation of Li^+, K^+, and Ca^{2+} effectively improves both the thermal robustness and emission efficiency of Yb^{3+}, Ho^{3+}:NBM crystals, offering valuable insights for the design of high-performance UC materials.

2. Experimental details

2.1. Crystal growth

A series of high-quality Yb^{3+}, Ho^{3+} co-doped NBM single crystals, with nominal concentrations of 5 at.% Yb^{3+} and 2 at.% Ho^{3+}, were successfully grown via the Czochralski (Cz) method. To investigate the influence of co-doping on luminescence behavior, an additional 10 at.% of Li^+, K^+, or Ca^{2+} ions was individually introduced into the melt. Crystal

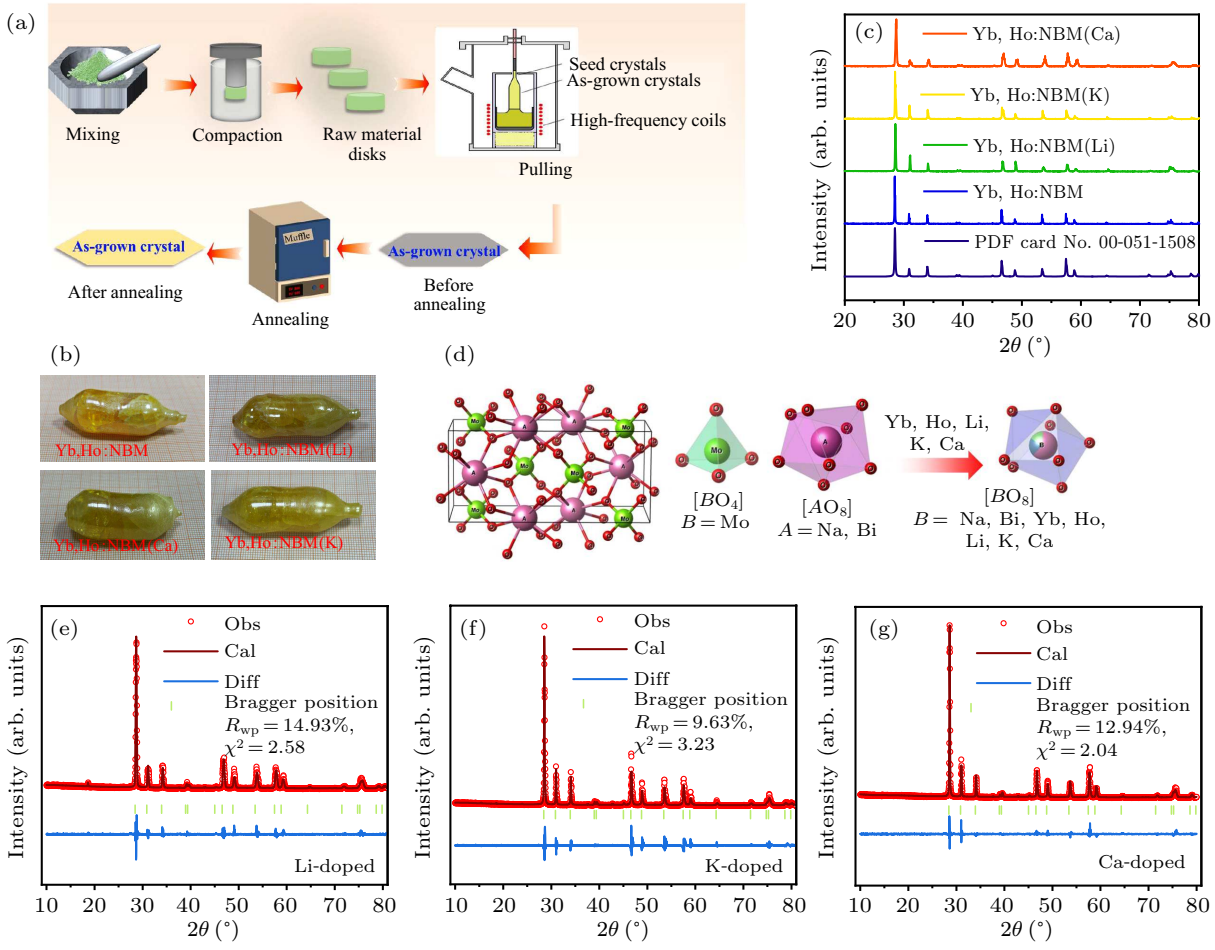


Fig. 1. (a) The process of crystal growth by the Czochralski method and annealing. (b) A series of as-grown Yb^{3+}, Ho^{3+}:NBM single crystals. (c) The XRD patterns of Yb^{3+}, Ho^{3+}:NBM crystals and those doped with Li^+, K^+, and Ca^{2+} ions, respectively. (d) Crystal structure and doping model of Yb^{3+}, Ho^{3+}:NBM. (e), (f) The Rietveld refinement results for the Li^+, K^+ and Ca^{2+} doped single crystals.

growth was conducted using a JGD-400 Cz furnace (CETC 26th Institute, China), equipped with an intermediate-frequency induction heating system and an automatic diameter control (ADC) module. Analytical-grade starting materials including Yb_2O_3 (99.99%), Ho_2O_3 (99.99%), Na_2CO_3 (99.99%), MoO_3 (99.99%), Bi_2O_3 (99.99%), Li_2CO_3 (99.99%), K_2CO_3 (99.99%), and $CaCO_3$ (99.99%) were obtained from Aladdin Reagent. These reagents were measured and weighed in line with their stoichiometric ratios, thoroughly mixed, and a 60 g batch was loaded into a platinum crucible for each growth trial. During the process, the pulling speed was kept at 1.5 mm per hour, while the seed rotation rate was maintained at 7 rpm. After crystal growth, a post-annealing step was employed to eliminate oxygen vacancies and improve optical quality. The as-grown crystals were then cooled down to room temperature at a rate of 30 W/h. Although some cracks were observed (Fig. 1(b)), the crystals retained sufficient integrity for subsequent structural and optical characterization. A schematic illustration of the crystal growth setup is shown in Fig. 1(a).

2.2. Characterization

The crystal structure of the as-grown samples was analyzed using a Bruker D8 Advance x-ray diffractometer with Cu $K\alpha$ radiation ($\lambda = 1.5406$ Å). X-ray diffraction (XRD) patterns were recorded over a 2θ range of 10°–80° with a step size of 0.02°. The surface morphology and elemental distribution of the samples were examined using a JSM-6510 scanning electron microscope (SEM). Photoluminescence measurements, including UC emission spectra and fluorescence lifetimes, were carried out using an Edinburgh instruments FLSP-920 spectrometer. A 980 nm semiconductor laser (BWT Beijing Ltd.) with a maximum output power of 10 W served as the excitation source for UC luminescence experiments.

3. Results and discussion

3.1. Crystal structure

Figure 1(c) presents the XRD patterns of Yb^{3+}, Ho^{3+} co-doped NBM single crystals with various alkali and alkaline earth dopants. All diffraction peaks are well indexed to the standard reference pattern (PDF#00-051-1508), indicating that the incorporation of Li^+, K^+, or Ca^{2+} ions does not significantly alter the tetragonal crystal structure of NBM. The corresponding structural model is illustrated in Fig. 1(d), where the NBM lattice adopts the $I4_1/a$ space group. The crystal framework consists of interconnected [Na/BiO_8] polyhedra and [MoO_4] tetrahedra, arranged in an irregular yet symmetric three-dimensional network. Within this structure, both Na^+ and Bi^{3+} ions are eightfold coordinated by oxygen atoms, forming distorted dodecahedra. Based on ionic radii and charge compensation considerations, it is proposed that the dopant ions K^+, Li^+, Ca^{2+}, Yb^{3+}, and Ho^{3+} substitute primarily at the Na^+ and Bi^{3+} sites, without inducing significant phase separation or secondary phases. The Rietveld refinement results (Figs. 1(e)–1(g)) for the Li^+, K^+, and Ca^{2+} doped single crystals also confirmed this result.

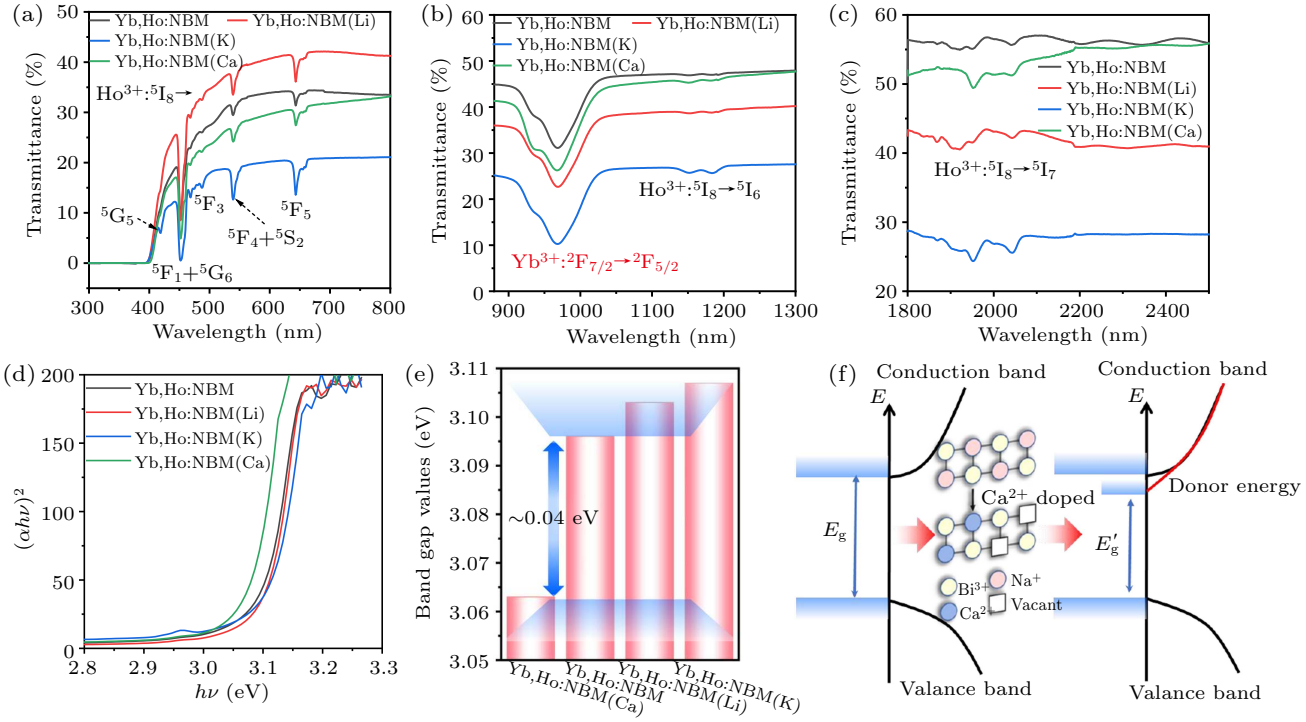


Fig. 2. (a)–(c) Transmittance of the crystals. (d) Tauc plot of the grown crystals. (e) Comparison diagram of the band gap values of the grown crystals. (f) Schematic diagram of bandgap narrowing caused by doping.

Figures 2(a)–2(c) show the optical transmittance spectra of the doped crystals. Prominent absorption valleys near 450 nm and 980 nm are attributed to the characteristic absorption of Ho^{3+} and Yb^{3+} ions, respectively. Specifically, the peaks at 450 nm, 546 nm, and 660 nm correspond to Ho^{3+} transitions from the ground state $^5I_8$ to the excited states $^5F_1+^5G_6$, $^5F_4+^5S_2$, and $^5F_5$, respectively. Additionally, the absorption band near 980 nm arises from the $^2F_{7/2} \rightarrow {}^2F_{5/2}$ transition of Yb^{3+}. We also observe features associated with intra-configurational transitions such as $^5I_8 \rightarrow {}^5I_6$ and $^5I_7$ of Ho^{3+}.

To estimate the optical band gap, the absorption data were fitted using Tauc's equation

$$(\alpha h\nu)^n = K\left(h\nu - E_g\right), \tag{1}$$

where α is the absorption coefficient, $h\nu$ is the photon energy, E_g is the optical bandgap, K is a constant, and n is 2 for direct and $1/2$ for indirect transitions.[27] Figures 2(d)–2(e) show the bandgap fitting results. Notably, the Ca^{2+}-doped crystal exhibits a bandgap approximately 0.04 eV narrower than its Li^+, K^+, and undoped counterparts. This narrowing is indicative of an extended absorption edge and improved photon utilization. The enhancement may originate from two mechanisms: (i) the valence mismatch between Ca^{2+} and RE^{3+} ions potentially induces local lattice shrinkage and modifies the surrounding field symmetry; and (ii) heavy Ca^{2+} doping (10 at.%) introduces discrete donor energy levels that overlap to form an impurity band, thereby reducing the effective bandgap and enhancing electronic transition probabilities.[28,29] As illustrated in Fig. 2(f), we propose that the observed bandgap narrowing arises from impurity band formation due to high-concentration Ca^{2+} donor states. These states coalesce to generate shallow defect bands within the host matrix, facilitating enhanced NIR absorption and ultimately contributing to improved UC luminescence performance.

3.2. UC luminescence properties

To comprehensively evaluate the optical properties of the doped NBM crystals, two luminescence mechanisms were investigated: (i) UC emission under 980 nm laser excitation (Fig. 3(a)) and (ii) photoluminescence under 450 nm excitation (Fig. 3(b)). As shown in Fig. 3(a), the UC emission spectra of four post-growth polished NBM single crystals reveal two pronounced emission bands centered at $\sim$ 550 nm and $\sim$ 650 nm under 980 nm excitation. These emissions correspond to the characteristic transitions of Ho^{3+} ions, specifically $^5F_4, {}^5S_2 \rightarrow {}^5I_8$ (green) and $^5F_5 \rightarrow {}^5I_8$ (red), respectively. Visibly, all samples exhibit intense red luminescence to the naked eye under NIR excitation. Conversely, strong green emission dominates when the crystals are excited at 450 nm, highlighting a stark excitation-dependent color contrast.

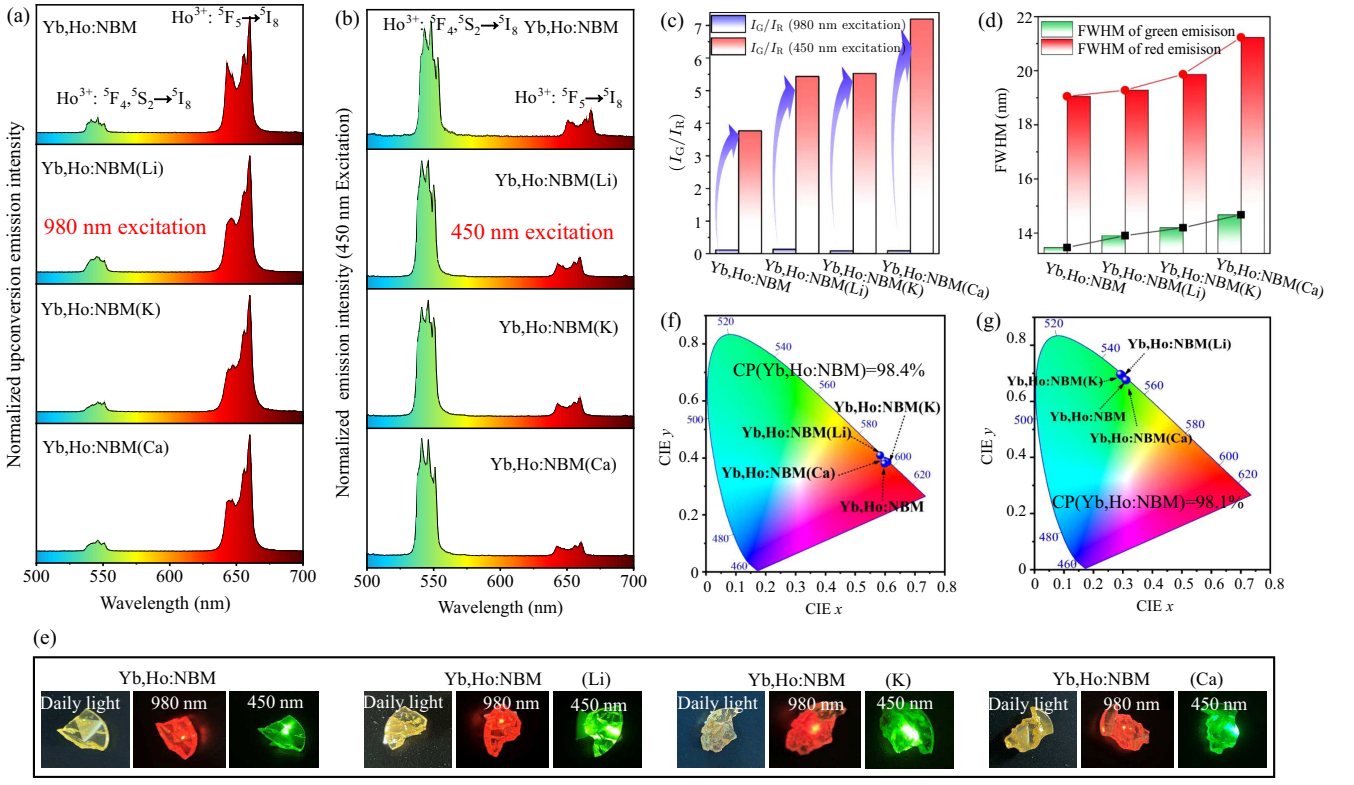


Fig. 3. (a), (b) Room temperature emission spectra under 980 nm and 450 nm excitations. (c) Histogram of green-to-red wavelength ratios under varied excitation wavelengths. (d) Full width at half maximum of different crystals. (f), (g) CIE chromaticity coordinates of crystals under varied excitation wavelengths. (e) Comparison diagram of crystal sheets under daily light, 980 nm excitation, and 450 nm excitation.

The emission intensity ratios of green-to-red components under 450 nm versus 980 nm excitation conditions are summarized in Fig. 3(c). The ratio increases markedly with doping, reaching values of 33 (undoped), 41 (Li^+), 66 (K^+), and 79 (Ca^{2+}), respectively. This pronounced spectral tunability indicates potential application in optical anti-counterfeiting, where dual-mode excitation can produce distinct luminescent responses. Figure 3(d) displays the full width at half maximum (FWHM) of both green and red emission bands. Compared to the undoped NBM crystal, the doped samples exhibit noticeable spectral broadening. This is attributed to increased lattice disorder induced by dopant ions, which disrupt the local crystal field environment and promote phonon interactions, thereby broadening the emission profile. Photographs of the crystal plates under 980 nm and 450 nm laser excitation are shown in Fig. 3(e). The respective red and green luminescence under different excitation wavelengths are visually evident. Additionally, the chromatic purity of the emissions was quantified and found to exceed 98% for all samples (Figs. 3(f)–3(g)), confirming the generation of highly saturated spectral colors.

Figure 4(a) presents the UC emission spectra of the doped crystals under various excitation power densities ranging from 0.1 W to 1 W. A steady increase in emission intensity is observed for both green and red bands without any spectral shift, indicating excellent spectral stability. To elucidate the multiphoton nature of the UC process, the dependence of integrated emission intensity (I) on pump power (P) was fitted using the following relationship:[30]

$$I \propto P^n, \tag{2}$$

$$\ln I \propto n \ln P, \tag{3}$$

where n represents the number of photons involved in the UC process.

Figure 3(b) shows the slope n obtained from linear fitting of the log–log plots. For all doped and undoped samples, $n \approx 2$ for both green and red emission bands, confirming a two-photon absorption mechanism in the Yb^{3+}, Ho^{3+}:NBM system. Moreover, the red-to-green emission ratio remains nearly constant as the excitation power increases (Fig. 3(c)), with minimal fluctuation (as low as 4.5%) observed in the alkali-metal-doped samples, underscoring the power-dependent emission stability of the crystals.

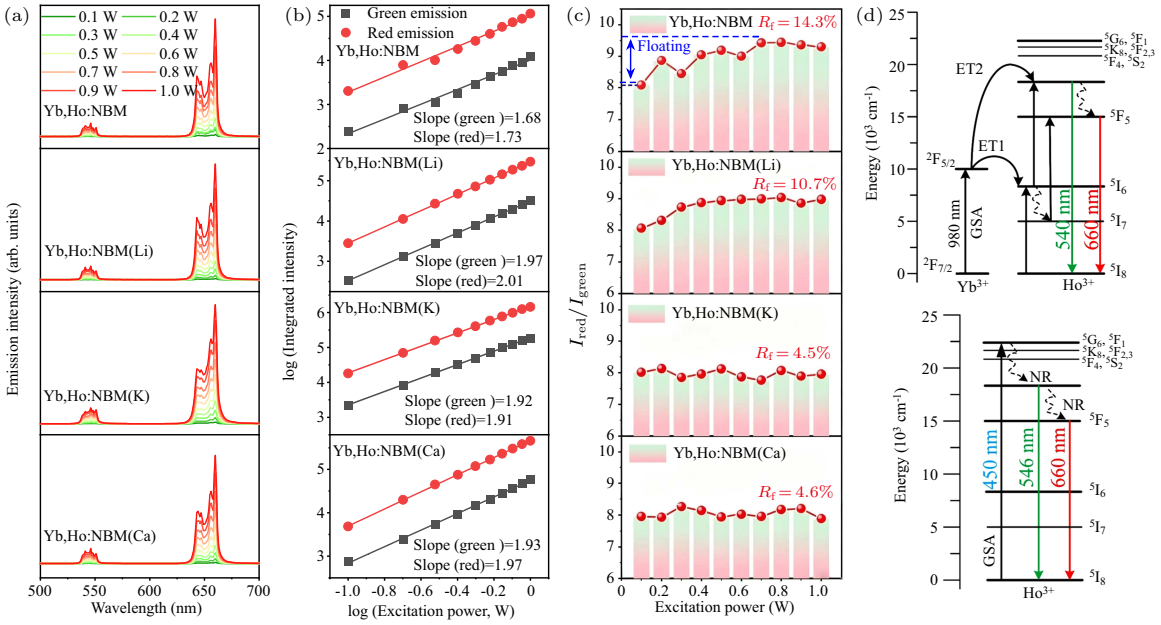


Fig. 4. (a) UC emission spectra of Yb^{3+}, Ho^{3+}: $NaBi(MoO_4)_2$ (doped Li^+, K^+, Ca^{2+}) crystal at varying excitation powers. (b) Log–log plots of pump power dependence of the UC emission intensity for the grown crystals. (c) Histogram of red-to-green intensity ratios under varied excitation power densities. (d) Energy levels of Yb and Ho and the possible UC processes.

The UC mechanism is schematically illustrated in Fig. 4(d). Under 980 nm excitation, incident photons are initially absorbed by Yb^{3+} ions through ground state absorption (GSA), promoting electrons from the $^2F_{7/2}$ to $^2F_{5/2}$ levels. These sensitizer ions transfer energy to Ho^{3+} activators via a two-step energy transfer process. The first transfer (ET1) populates the Ho^{3+} $^5I_6$ state from the $^5I_8$ ground state, while the second transfer (ET2) excites electrons to the $^5F_4$, $^5S_2$ manifold, from which radiative relaxation to $^5I_8$ produces green emission (∼ 540 nm). Non-radiative relaxation from $^5F_4$, $^5S_2$ to $^5F_5$ further enables red emission (∼ 660 nm) via $^5F_5 \rightarrow {}^5I_8$ transition.

3.3. UC luminescence thermal stability

To evaluate the thermal stability of the as-grown NBM crystals, temperature-dependent UC emission spectra were recorded over a temperature range of 300 K to 540 K under 980 nm laser excitation. As shown in Fig. 5(a), a gradual de-

crease in overall emission intensity is observed with increasing temperature. However, the spectral shape and peak positions remain largely unchanged, indicating that the radiative transitions remain stable during thermal cycling. Two characteristic Ho^{3+} emission bands, centered at 540 nm ($^5F_4$,$^5S_2 \rightarrow {}^5I_8$) and 660 nm ($^5F_5 \rightarrow {}^5I_8$), are clearly sustained throughout the temperature range. Among the tested samples, the Ca^{2+}-doped Yb^{3+}, Ho^{3+}:NBM crystal displays good thermal quenching resistance. This enhanced stability is evident from the preserved emission intensity at elevated temperatures. Quantitative analysis of integrated emission intensity is presented in Fig. 5(c). Compared to the Li^+- and K^+-doped counterparts, the Ca^{2+}-doped crystal retains a significantly higher proportion of its initial emission intensity. Notably, at 500 K, the Ca^{2+}-doped crystal maintains 48.6% of its room-temperature emission intensity, underscoring its enhanced thermal robustness. To further assess the thermal repeatability and structural stability of the crystals under high-temperature conditions, multiple thermal cycling experiments were performed between 300 K and 540 K. The corresponding results are depicted in Figs. 5(b) and 5(d). The emission intensity profiles remain stable across successive heating and cooling cycles, confirming that the as-grown NBM crystals exhibit excellent thermal durability and structural reversibility. These findings collectively demonstrate that alkali and alkaline earth metal

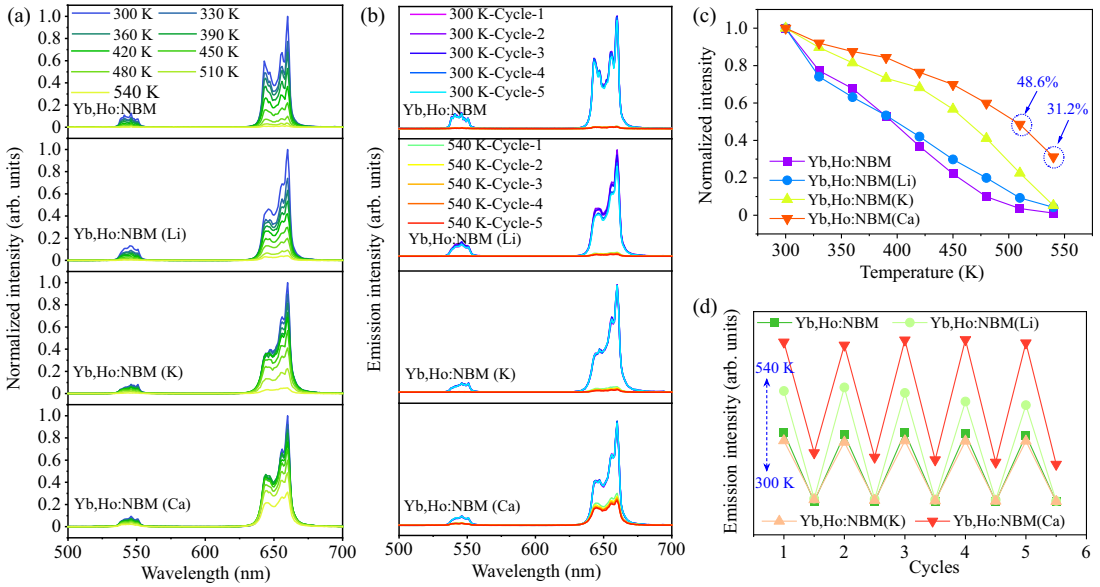


Fig. 5. (a) Temperature-dependent UC emission spectra of crystals at different temperatures (300–540 K) under 980 nm excitation. (c) The line chart of the integrated results of luminous intensity of each crystal at different temperatures. (b) and (d) Thermometer reliability of the crystals during multiple heating–cooling cycles in the temperature range of 300–540 K.

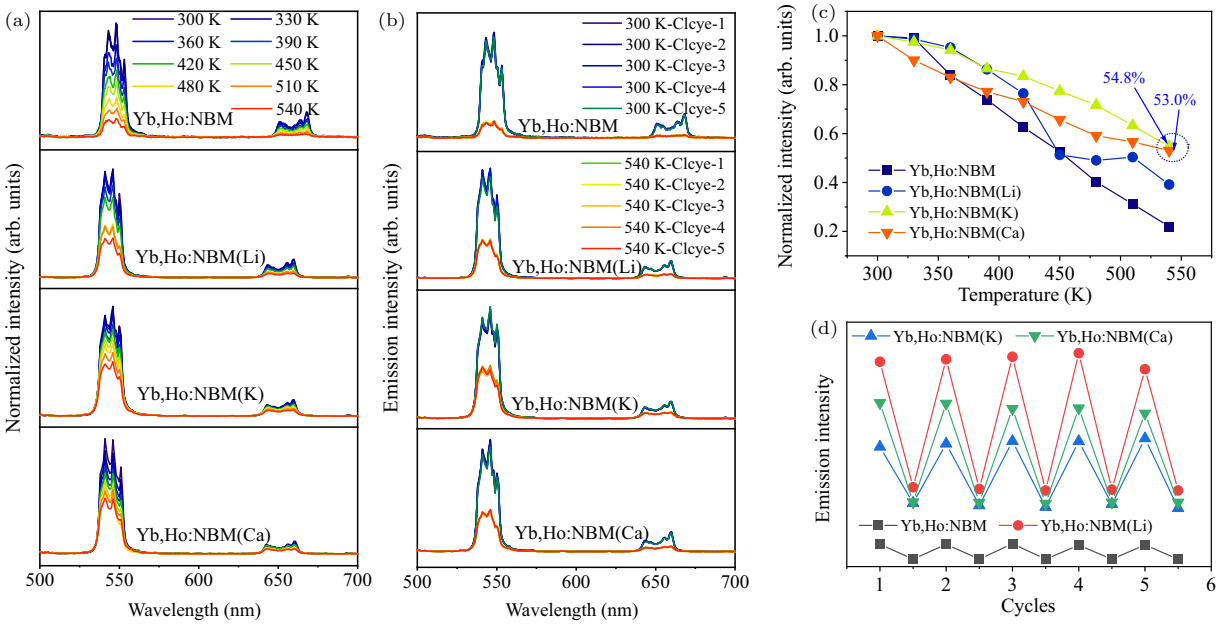


Fig. 6. (a) Temperature-dependent emission spectra of crystals at different temperatures (300–540 K) under 450 nm excitation. (c) The line chart of the integrated results of luminous intensity of each crystal at different temperatures. (b) and (d) Thermometer reliability of the crystals during multiple heating–cooling cycles in the temperature range of 300–540 K.

ion doping, particularly with Ca^{2+}, can effectively suppress thermal quenching and improve the temperature resilience of UC luminescence. The observed enhancements are attributed to modified local crystal field symmetry and reduced non-radiative transition probabilities, making these materials promising candidates for temperature-sensitive photonic applications.

To expand the application scenarios of the as-grown crystals, we also investigated the temperature-dependent UC spectra of the crystals under 450 nm excitation. Figure 6(a) presents the temperature-dependent UC spectra under 450 nm excitation, revealing a significantly dominant emission peak at 546 nm compared to that at 660 nm, indicative of pronounced green emission. The disparity in emission color between 980 nm and 450 nm excitation regimes has been mechanistically elucidated in our previous work.[31] Consistent with the methodology employed for 980 nm excitation, we constructed the integrated intensity plot shown in Fig. 6(c). Ca^{2+}-doped Yb^{3+}, Ho^{3+}:NBM crystals exhibit exceptional thermal robustness, retaining around 53% of their room-temperature emission intensity at 540 K. The thermal cycling test results presented in Figs. 6(b) and 6(d) show that the synthesized crystals exhibit good thermal cyclic repeatability.

3.4. Fluorescence decay curves

Figures 7(a) and 7(b) present the luminescence decay profiles of Yb^{3+}, Ho^{3+}:NBM crystals and their Li^+, K^+, and Ca^{2+} co-doped counterparts. The surface of the samples was excited with a laser diode with emission peak center at $\lambda =$ 450 nm, and the emission was monitored from the transitions Ho^{3+}: $^5F_4$,$^5S_2 \rightarrow {}^5I_8$ (546 nm) and Ho^{3+}: $^5F_5 \rightarrow {}^5I_8$ (660 nm). The lifetime was computed by applying a double exponential function to fit the decay curves, utilizing the equation provided below:[25]

$$I = A_1 \exp\left(-\frac{t}{\tau_1}\right) + A_2 \exp\left(-\frac{t}{\tau_2}\right), \tag{4}$$

where t is the decay time of the $^5F_4$,$^5S_2$ and $^5F_5$ level of Ho^{3+}. I and I_0 represent the emission intensities at time t and 0, respectively. The decay curves showed a good fit with a double exponential function, as shown in Figs. 7(c) and 7(d). The average lifetime (τ_{ave}) was obtained according to the following expression:

$$\tau_{ave} = \frac{A_1\tau_1^2 + A_2\tau_2^2}{A_1\tau_1 + A_2\tau_2}. \tag{5}$$

As shown in Figs. 7(e) and 7(f), the luminescence lifetimes of all tested crystals exhibit a progressive reduction with increasing temperature. As reported in the literature,[32] this phenomenon arises from enhanced lattice vibrations at elevated temperatures, which intensify electron–phonon interactions and amplify nonradiative transitions, consequently shortening the luminescence lifetime. In addition, it can also be seen from Figs. 7(c) and 7(d) that doping with either alkaline earth or alkali metals has a certain effect in suppressing lifetime decay. Among them, the Yb^{3+}, Ho^{3+}:NBM crystal doped with Ca^{2+} ions exhibits the best thermal stability, and its lifetime decays most slowly during the temperature change from 300 K to 540 K.

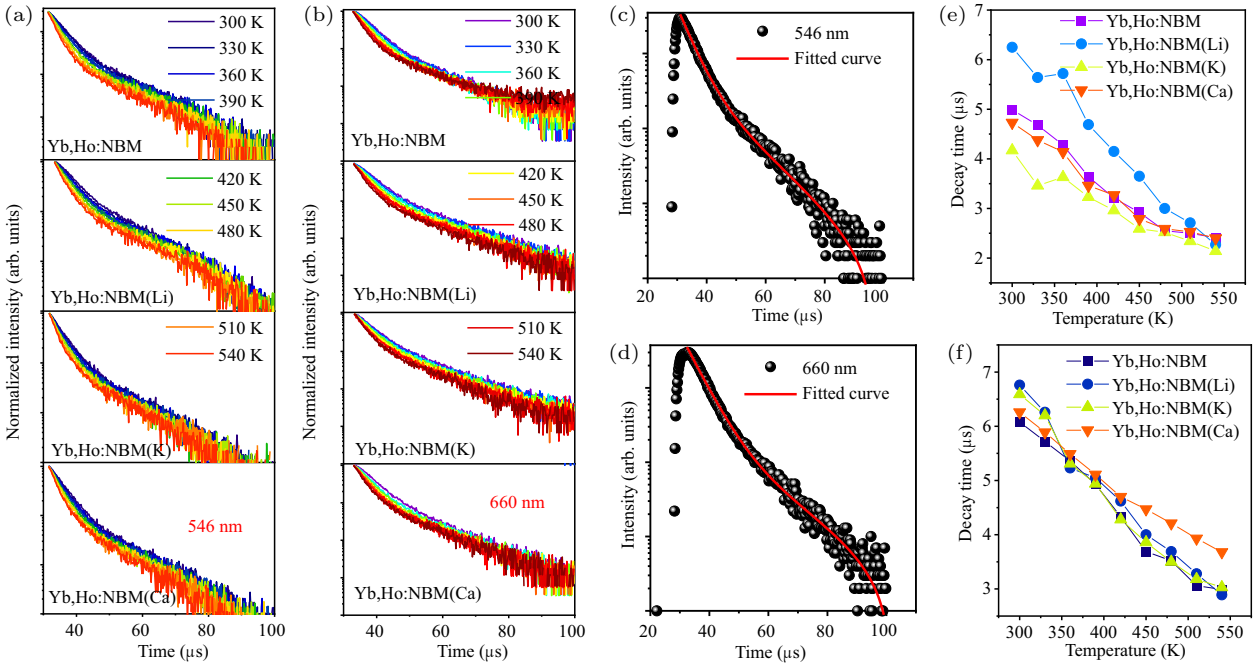


Fig. 7. (a), (b) Luminescence decay curves of Yb^{3+}, Ho^{3+}:NBM crystals and their co-doped Li^+, K^+, and Ca^{2+} crystals at different temperatures. (c), (d) Biexponential fitting results of the fluorescence decay curves monitored at 546 nm and 660 nm at room temperature. (d) Relationship between the crystal lifetime and temperature under 450 nm excitation and 546 nm monitoring. (e) Relationship between the crystal lifetime and temperature under 450 nm excitation and 660 nm monitoring.

4. Conclusion

In summary, a series of Yb^{3+}, Ho^{3+} co-doped NBM single crystals, further modified with Li^{+}, K^{+}, and Ca^{2+} ions, were successfully grown using the Czochralski method. Structural characterization via x-ray diffraction, transmission spectroscopy, and scanning electron microscopy confirmed that all samples crystallize in a tetragonal scheelite-type structure (space group $I4_1/a$). Under dual-mode laser excitation at 980 nm and 450 nm, the crystals exhibited distinct emission profiles dominated by red and green luminescence, respectively. Ca^{2+} doping was shown to induce donor-level formation and bandgap narrowing, as revealed by Tauc plot analysis. The incorporation of alkali and alkaline earth metal ions significantly enhanced the green-to-red emission ratio and broadened the full width at half maximum (FWHM), indicating increased lattice disorder and local symmetry distortion. Power-dependent UC studies confirmed that both red and green emissions arise from two-photon excitation processes. Temperature-dependent luminescence measurements under both excitation regimes demonstrated that Li^{+}, K^{+}, and Ca^{2+} doping effectively mitigates thermal quenching. In particular, the Ca^{2+}-doped samples exhibited the highest thermal robustness, retaining over 50% of room-temperature emission intensity at elevated temperatures. Overall, this study demonstrates that co-doping with Li^{+}, K^{+}, and Ca^{2+} ions not only improves the UC luminescence intensity but also significantly enhances the thermal stability of Yb^{3+}, Ho^{3+}:NBM crystals. These findings provide valuable insights into the design of high-performance luminescent materials for thermally demanding optoelectronic and anti-counterfeiting applications.

Acknowledgements

This work was supported by the Natural Science Research Project of Anhui Province Education Department for Excellent Young Scholars (Grant No. 2024AH030007) and the National Natural Science Foundation of China (Grant No. 52202001).

References

[1] Auzel F 2004 *Chem. Rev.* **104** 139
[2] Chen G Y, Qiu H L, Prasad P N and Chen X Y 2014 *Chem. Rev.* **114** 5161
[3] Ding M Y, Dong B, Lu Y, Yang X F, Yuan Y J, Bai W F, Wu S T, Ji Z G, Lu C H, Zhang K and Zeng H B 2020 *Adv. Mater.* **32** e2002121
[4] Liu J X, Zha J L, Yang Y L, Lu X M, Hu X L, Yan S, Wu Z J and Huang F Z 2024 *Chin. Phys. Lett.* **41** 077701
[5] Niu Y D, Wang Y Z, Zhu K M, Ye W G, Feng Z, Liu H, Yi X, Wang Y H and Yuan X Y 2023 *Chin. Phys. B* **32** 028703
[6] Lu Z Y, Chen L T, Hu X, Chen S Y, Zhang X and Zhou Z 2024 *Chin. Phys. Lett.* **41** 127302
[7] Trupke T, Green M A and Würfel P 2002 *J. Appl. Phys.* **92** 1668
[8] De Rijke F, Zijlmans H, Li S, Vail T, Raap A K, Niedbala R S and Tanke H J 2001 *Nat. Biotechnol.* **19** 273
[9] Wang F and Liu X 2009 *Chem. Soc. Rev.* **38** 976
[10] Mahata M K, Koppe T, Mondal T, Brüsewitz C, Kumar K, Kumar Rai V, Hofsäss H and Vetter U 2015 *Phys. Chem. Chem. Phys.* **17** 20741
[11] Guler I, Isik M and Gasanly N M 2024 *Appl. Phys. A* **130** 625
[12] Kshetrapal S, Ugemuge N S, Sharma K, Nafdey R and Moharil S V 2024 *J. Opt.* **54** 1430
[13] Gan Y, Liu W, Zhang W T, Li W J, Huang Y and Qiu K H 2019 *J. Alloys Compd.* **784** 1003
[14] Volkov V, Rico M, MeÂndez-Blas A and Zaldo C 2002 *J. Phys. Chem. Solids.* **63** 95
[15] Tsydypova B N, Gusakova N V, Pavlyuk A A, Yasyukevich A S, Kuleshov N V, Grigor'ev S V and Solodovnikov S F 2014 *Inorg. Mater.* **50** 617
[16] Rico M, Volkov V and Zaldo C 2001 *J. Alloys Compd.* **323–324** 806
[17] Cascales C, Méndez Blas A, Rico M, Volkov V and Zaldo C 2005 *Opt. Mater.* **27** 1672
[18] Rinkel T, Raj A N, Duhnen S and Haase M 2016 *Angew Chem. Int. Ed. Engl.* **55** 1164
[19] Yadav R V, Singh S K and Rai S B 2015 *RSC Adv.* **5** 26321
[20] Qian Y N, Wang R, Wang B, Xu C, Xu W, Xing L L and Xu Y L 2013 *J. Quant. Spectrosc. Radiat. Transfer.* **129** 60
[21] Balakrishna A and Ntwaeaborwa O M 2017 *Sens. Actuators, B.* **242** 305
[22] Mukhopadhyay L, Rai V K, Bokolia R and Sreenivas K 2017 *J. Lumin.* **187** 368
[23] Vidyakina A A, Kolesnikov I E, Bogachev N A, Skripkin M Y, Tumkin, I I, Lahderanta E and Mereshchenko A S 2020 *Materials (Basel).* **13** 3397
[24] Maurya A, Bahadur A, Dwivedi A, Choudhary A K, Yadav T P, Vishwakarma P K and Rai S B 2018 *J. Phys. Chem. Solids.* **119** 228
[25] Maurya A, Yadav R S, Yadav R V, Rai S B and Bahadur A 2016 *RSC Adv.* **6** 113469
[26] Liu L, Wang Y X, Bai Y F, Zhang X R, Yang K and Song Y L 2012 *Appl. Phys. B* **110** 111
[27] Xia M, Gu S M, Zhou C, Liu L H, Zhong Y, Zhang Y L and Zhou Z 2019 *RSC Adv.* **9** 9244
[28] Astha K, Anurag P, Riya D and Rai V K 2014 *RSC Adv.* **4** 21844
[29] Shannon R D 1976 *Acta Cryst.* **A32** 751
[30] Pollnau M, Gamelin D R, Lüthi S R, Güdel H U and Hehlen M P 1999 *Phys. Rev. B* **61** 3337
[31] Su W Z, Zhang M Y, Zhang C C, Zou Y, Liu W P and Ding S J 2025 *J. Mol. Struct.* **1343** 142855
[32] Yu W, Xu W, Song H W and Zhang S 2014 *Dalton Trans.* **43** 6139